Journal of Neuroradiology 46 (2019) 179–185

Available online at ScienceDirect www.sciencedirect.com

Elsevier Masson France EM|consulte www.em-consulte.com

Original article

Radiomic biomarkers informative of cancerous transformation in neurofibromatosis-1 plexiform tumors☆

J. Uthoff[a,b], F.A. De Stefano[a], K. Panzer[c], B.W. Darbro[c], T.S. Sato[a], R. Khanna[d], D.E. Quelle[e], D.K. Meyerholz[f], J. Weimer[g], J.C. Sieren[a,b,*]

[a] Department of Radiology, University of Iowa, Iowa City, Iowa, United States of America
[b] Department of Biomedical Engineering, University of Iowa, Iowa City, Iowa, United States of America
[c] Department of Pediatrics, University of Iowa, Iowa City, Iowa, United States of America
[d] Department of Pharmacology, University of Arizona, Arizona, United States of America
[e] Department of Pharmacology, University of Iowa, Iowa City, Iowa, United States of America
[f] Department of Pathology, University of Iowa, Iowa City, Iowa, United States of America
[g] Pediatric and Rare Disease Group, Sanford Research, Sioux Falls, South Dakota, United States of America

ARTICLE INFO

Article history:
Available online 27 June 2018

Keywords:
Malignant peripheral nerve sheath tumor
Plexiform neurofibroma
Magnetic resonance imaging
Positron emission tomography
Quantitative feature extraction

ABSTRACT

Background. – This study explores whether objective, quantitative radiomic biomarkers derived from magnetic resonance (MR), positron emission tomography (PET), and computed tomography (CT) may be useful in reliably distinguishing malignant peripheral nerve sheath tumors (MPNST) from benign plexiform neurofibromas (PN).
Methods. – A registration and segmentation pipeline was established using a cohort of NF1 patients with histopathological diagnosis of PN or MPNST, and medical imaging of the PN including MR and PET-CT. The corrected MR datasets were registered to the corresponding PET-CT via landmark-based registration. PET standard-uptake value (SUV) thresholds were used to guide segmentation of volumes of interest: MPNST-associated PET-hot regions (SUV $\geq$ 3.5) and PN-associated PET-elevated regions (2.0 < SUV < 3.5). Quantitative imaging features were extracted from the MR, PET, and CT data and compared for statistical differences. Intensity histogram features included (mean, media, maximum, variance, full width at half maximum, entropy, kurtosis, and skewness), while image texture was quantified using Law's texture energy measures, grey-level co-occurrence matrices, and neighborhood grey-tone difference matrices.
Results. – For each of the 20 NF1 subjects, a total of 320 features were extracted from the image data. Feature reduction and statistical testing identified 9 independent radiomic biomarkers from the MR data (4 intensity and 5 texture) and 4 PET (2 intensity and 2 texture) were different between the PET-hot versus PET-elevated volumes of interest.
Conclusions. – Our data suggests imaging features can be used to distinguish malignancy in NF1-realted tumors, which could improve MPNST risk assessment and positively impact clinical management of NF1 patients.

Introduction

Neurofibromatosis-1 (NF1) is an autosomal dominant genetic condition affecting 1 in 3500 individuals worldwide with a diverse number of clinical manifestations [1]. The diagnostic criteria for NF1, established by the National Institute of Health Consensus Development Panel (NIH-HCD), includes presence of neurofibromas [2]. Internal neurofibromas and plexiform neurofibromas (PNs) can cause disfigurement and have the potential to transform into malignant peripheral nerve sheath tumors (MPNST). These lesions are of particular concern for NF1 patients as the five year survival rate for these individuals is reported as 20–50% [3].

Most NF1-related MPNSTs arise from pre-existing PNs; therefore, subjects with known PNs are often evaluated clinically with longitudinal magnetic resonance (MR) imaging to assess tumor growth and heterogeneity changes [4]. When malignancy is suspected, [^{18}F] 2-fluoro-2-dexoy-D-glucose (^{18}F-FDG) positron

☆ We would like to thank the financial support of the Children's Tumor Foundation NF1 Synodos Grant (2015-18-002 C).
* Corresponding author. 200, Hawkins Dr. CC704GH, 52242 Iowa City Iowa, United States of America.
E-mail address: jessica-sieren@uiowa.edu (J.C. Sieren).

https://doi.org/10.1016/j.neurad.2018.05.006
0150-9861/

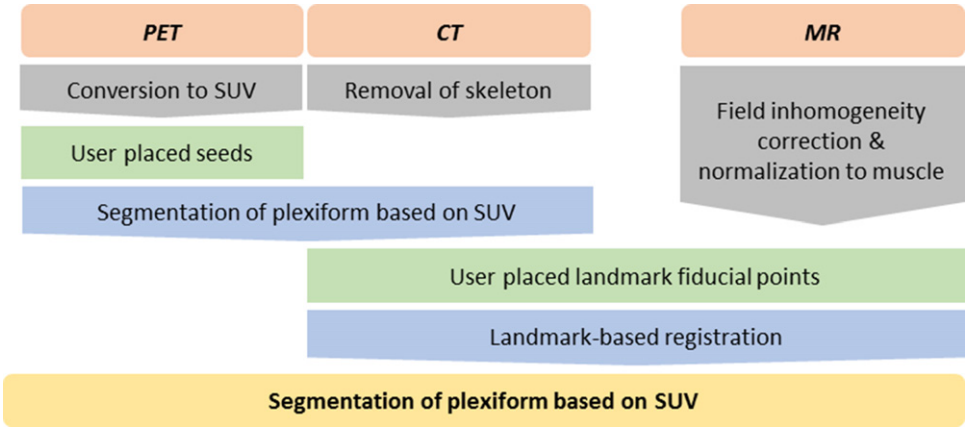

Fig. 1. Overview of the plexiform segmentation pipeline for PET-CT and MR datasets.

emission tomography computed tomography (PET-CT) is used as a non-invasive procedure to detect tissue transformation [5,6]. PET-CT uses standard-uptake value (SUV) to relate the acquired PET-signal to the functional uptake of the radiotracer in tissues. Tumor SUV_{max} calculations are incorporated into clinical decision making for the differentiation between MPNST and benign plexiform neurofibroma (BPN). To standardize this method, studies have been conducted to define relevant SUV_{max} threshold values [6–8]. A review by Treglia demonstrated a range in SUV_{max} cut-off values (1.8–6.1) for PET-CT benefit; this review recommended a SUV_{max} of 3.5 or above as optimal for defining MPNST regions [6]. One caveat is the effect of time between ^{18}F-FDG radiotracer injection and PET scanning, which can range widely (45 to 240 minutes) [6]. To assess PN burden and examine relative malignancy risk, Salamon used three SUV cut-offs, 2.0, 2.5, and 3.5, to segment PN in PET-CT and calculate metabolic tumor volume [5]. These thresholds can be used to segment the PET-signal of a PN into three distinct groups: PET-hot ($SUV \geq 3.5$), PET-elevated ($2.0 \leq SUV < 3.5$), and background ($SUV < 2.0$).

Until this point, imaging-related NF1 research has focused on tumor volume assessment [9–11] and radiologists' qualitative analyses[12–16]. While semantic features are natural for radiologists to assign to lesions, there are inherent limitations related to the observation level of the human eye and reader subjectivity. The nature of medical imaging allows for numerous quantitative features to be defined using mathematical measures to describe image characteristics on the voxel level. Yip investigated the association between radiologist-defined qualitative and automated radiomic features in non-small cell lung cancer and found weak to moderate correlation between quantitative radiomic features and semantic features [17]. Quantitative radiomics, being derived directly from the imaging data, have the benefit of consistently providing the same values for image characteristics and can be integrated into a machine learning approach for disease assessment.

This study explores whether a tumor segmentation guided by SUV intensity contains quantitative MR and PET-CT radiomic biomarkers which are informative of malignancy status. We predict quantitative imaging features exist in MR, CT, and PET which are different between PET-hot regions of MPNST and PET-elevated regions of PN. As such, these radiomic biomarkers could positively contribute to MPNST risk assessment in future machine learning applications. Here, we make the assumption PET-hot segmentations correspond to MPNST regions and PET-elevated segmentations correspond to PN regions. To explore this relationship further, we also examine how the quantitative imaging features of PET-elevated regions (PN) in subjects with MPNST resemble the features of PET-elevated regions in BPN subjects.

Materials and methods

Retrospective cohort development

With Institutional Review Board approval, potential subjects were identified by the University of Iowa Hospitals and Clinics' Neurofibromatosis Clinic. Subject demographics, imaging history, and surgical pathology records were recorded. PET-CT and MR imaging sets, with accompanying radiology reports, were collected and anonymized with subject study identifiers. Inclusion criteria for this study were:

- NF1 patient with PN;
- histopathology diagnosis of either MPNST or BPN and;
- PET-CT and MR of PN within 1 year prior to histopathological diagnosis.

Segmentation pipeline development

The pipeline for PN identification was developed in-house using the Insight Toolkit (www.itk.org/) interfacing with the medical imaging visualization suite, Slicer (www.slicer.org/) [18,19]. To briefly summarize the process of feature extraction: automated pre-processing steps were performed on each scan to prime data for combination. Seed points were selected by the user to indicate both the PN location in PET and corresponding landmarks in CT and MR. Thresholding was applied to the PET scan to isolate SUV zones of the PN. Once aligned, the SUV mask was applied to CT and MR generating a scan-translational image set. A graphical overview of the segmentation process is detailed in Fig. 1.

The pre-processing steps included conversion of the raw PET data to SUVs and the removal of signal from the skeletal system using the accompanying CT data. The raw PET data was converted to SUVs using the patient specific SUV scaling. The mathematical formulation for the SUV voxel-wise conversion is shown in Equation (1), where the voxel value is the raw PET counts of radioactive events, actual activity is the injected radiotracer activity at time of scan, and the dose calibration factor is a measure of scanner efficiency:

$$SUV\left(\frac{kg}{mL}\right) = \frac{voxel\ \ value}{\left(\frac{actual\ \ activity}{body\ \ weight}\right) + \left(dose\ \ calibration\ \ factor + 10^6\right)} \quad (1)$$

Zones of similar uptake were generated from seed points placed in SUV intensive areas of the PN. A three-dimensional, 26-neighboorhood, connected thresholding filter was applied using

Table 1
Subject demographics including NIH's NF1 diagnostic criteria.

	MPNST [9]	BPN [17]	All [26]	NF1 Population [2]
Sex				
Female	2	6	8	~
Male	7	11	18	~
Café au lait	89%	100%	96%	99%
Lisch nodule	22%	29%	24%	95%
Optic glioma	22%	7%	15%	15%
Plexiform neurofibroma	100%	100%	100%	50%
Axillary or inguinal freckling	67%	88%	81%	85%
First-degree relative with NF1	44%	53%	50%	50%
Suv_{max}	6.8	3.0	4.9	~
Age	22 ± 16	22 ± 8	22 ± 14	~
Location	6I:3P	12I:5P	18I:8P	~
Maximum Diameter, (cm)	7.3 ± 3.6	6.7 ± 2.5	7.1 ± 3.2	~

MPNST: malignant peripheral nerve sheath tumor; BPN: benign plexiform tumor; F: female; M: male; I: internal; P: peripheral.

these seed points to generate the SUV-based PN mask. Based on literature, a SUV $\geq$ 3.5 was selected to be the threshold for an intensive uptake (PET-hot), while a SUV between 2.0 and 3.5 was selected to be the threshold for a moderate uptake (PET-elevated) [5].

The MR scans were pre-processed to correct for signal intensity inhomogeneity caused by magnetic field imperfections using a multiplicative bias field correction of the log-transformed dataset [20]. Intensity standardization is required in MR imaging for meaningful comparisons between different scan acquisitions or subjects; the voxel values in the MR scans were normalized to muscle values within the same scan [21]. Using a set of user-placed, skeletal fiducial points, the PET-CT and MR series were aligned through rigid registration [22]. This pipeline resulted in four volumes of interest (VOIs): a CT and an MR corresponding to the PET-hot region and a CT and an MR corresponding to the PET-elevated region. Tissue without a connected PET-elevated signal (SUV < 2.0) was designated as normal, non-plexiform tissue and excluded from feature analysis.

Quantitative imaging feature extraction and assessment

Two classes of quantitative imaging features were extracted: intensity histogram and image texture feature. Intensity histogram features are common values computed in image processing. In addition, four measures of heterogeneity were extracted from the histogram: full width at half maximum, entropy, kurtosis, and skewness. Image texture was quantified using Law's texture energy measures (LTEM), grey-level run length (GLRL), and neighborhood grey-tone difference matrices (NGTM) [23–25].

A statistical analysis module was used to determine difference between zones of the plexiform. Normality of the feature was tested using the Jarque-Bera normality test and the Levene's test was used to test for equal variances between the sets [26,27]. A Student's paired *t*-test compared the quantitative imaging features extracted from the PET-hot VOI to the PET-elevated VOI in the MPNST subjects. A second test was performed to compare the PET-elevated zones of MPNST and BPN subjects. Statistical significance was defined a $P < 0.05$. The correlated significant features can increase the final number of selected features with no new information gained; therefore feature reduction was performed using k-medoid clustering to remove statistically significant features were highly inter-correlated [28]. Statistical power test was performed for each of the significant features to check the sample size was adequate for the performed test (Statistical Solutions, LLC).

Results

Retrospective cohort

A cohort of 26 patients met the study inclusion criteria. Table 1 provides the demographics of these subjects including the prevalence of the NIH-HDC NF1 clinical diagnostic features. This cohort followed similar trends to the full NF1 population [2]. Of the 26, nine subjects had histopathology confirmed MPNST. One of these MPNST patients was excluded from PET-based segmentation as the subject's PN had a SUV_{max} of 3.4 which prevented segmentation using the pipeline. The remaining 17 subjects were histopathological BPNs; five of which were excluded from PET-based segmentation as their SUV_{max} was below the lower threshold of 2.0. Supplemental Table 1 displays the SUVmax, and semantic radiologic MR features (from the literatures – references) as recorded in the clinical radiology report for each case.

The PET-CT scans were performed using Siemens Biograph 64 scanner with parameters consistent across the cohort. Average ^{18}F-FDG radiotracer dose was 8.6 mCi (MPNST: 8.5 mCi, BPN: 8.7 mCi) with time post-injection to scanning ranged from 82–110 minutes (mean all: 93, MPNST: 94, BPN: 93). The scanning protocols of the MR datasets, on the other hand, were more variable. While all subjects had a local T1 (TR, 400–729 ms; TE, 7–12 ms; flip angle, 90–180°; echo train length, 1–3) and T2 (TR: 3800–8950 ms; TE: 86–122 ms; flip angle: 150–180°; echo train length: 17–27) MR of PN performed on a Siemens 1.5 Tesla, the plane of acquisition – axial, sagittal, or coronal – was not consistent across the cohort. The MR datasets also had a much higher in-plane resolution (mean: 0.24 mm × 0.24 mm) than the PET-CT scans (mean: 2.0 mm × 2.0 mm). This is common as MR is an anatomical scan while FDG PET-CT offers a view of function – i.e., glucose utilization. The subjects' MR imaging was generally acquired farther apart from pathology (mean: 52 ± 30 days) than the PET-CT imaging (mean: 22 ± 18 days).

Plexiform segmentation.

A total of 20 tumors (8 MPNST, 12 BPN) were processed through the segmentation pipeline resulting in 8 PET-hot and 20 PET-elevated masks. The alignment of PET-CT and MR data performed well in all abdominal plexiform subjects; however, for the few patients with PN on the limbs it proved more challenging as patient position varied between the two scans. Fig. 2 shows results of alignment and segmentation of three subjects: a well-circumscribed MPNST in the forearm, a diffuse MPNST in the pelvis, and a well-circumscribed BPN in the pelvis.

The remaining 6 tumors were manually segmented using Slicer's editor module. As the PET-signal for these cases prevented systemic

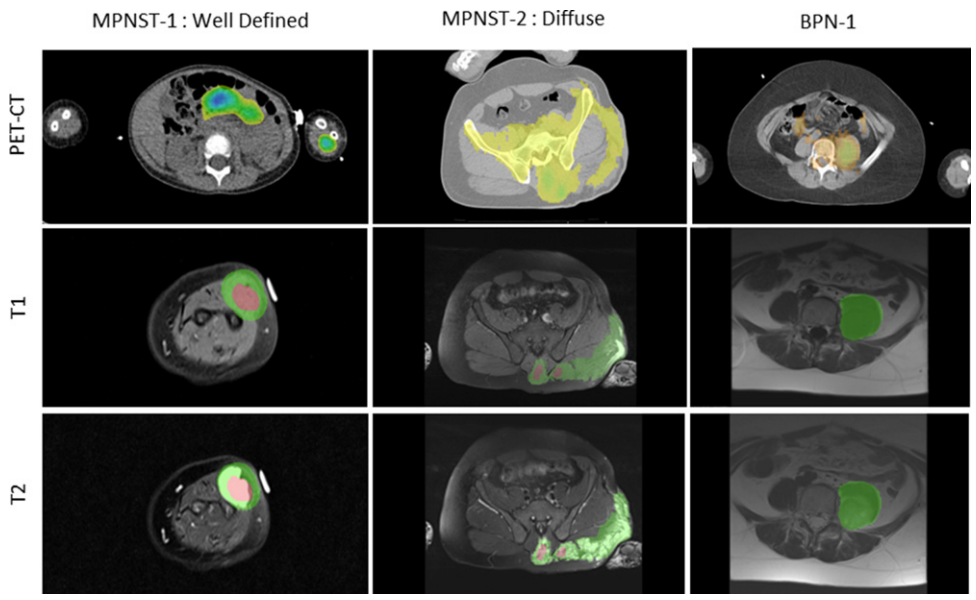

Fig. 2. Example cases for visualization: a well-circumscribed MPNST in the forearm, a diffuse MPNST in the pelvis, and a well-circumscribed benign PN (BPN) in the pelvis. Displayed are the PET-CT with associated colored SUVs (top row) and the T1 (middle row) and T2 (bottom row) MR scans with overlay masks. In the overlay masks the PET-hot regions is red and PET-elevated regions are green. The BPN subject did have a high fat signal in MR.

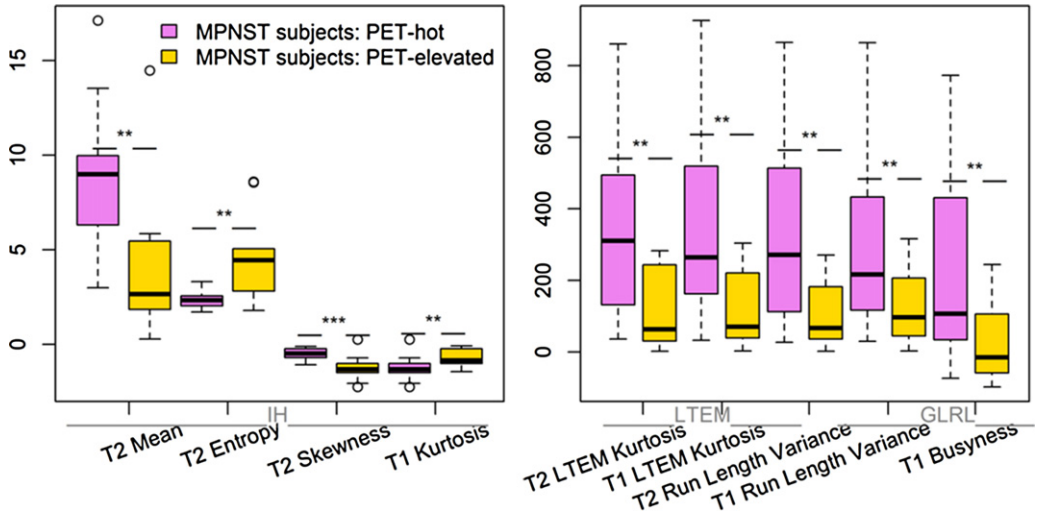

Fig. 3. Box-plots representation of significant MR features between PET-elevated regions of subjects with MPNST versus PET-elevated regions of subjects with BPN. Image texture features (Law's texture energy measures [LTEM], grey-level run length texture [GLRL], and neighborhood grey-tone matrix texture [NGTM]) were extracted from the normalized dataset, these texture features do not typically have units associated with them. The six cases with invalid segmentation PET-signal are shown with coordinated x's. Significance: $^{*}0.02 < P \leq 0.05$, $^{**}0.005 < P \leq 0.02$, $^{***}P \leq 0.005$.

segmentation, the cases were not used in determining statistically significantly different features between PET-zones. Instead, the subjects were used as an independent validation of differences found between MPNST and BPN PET-elevated regions – indicated with x's in Fig. 3.

Quantitative imaging features

The pipeline extracted 80 quantitative imaging features from each image dataset (T1 MR, T2 MR, PET and CT) resulting in a total of 320 features. From the paired *t*-test on the nine MPNST subjects, 21 quantitative imaging features (4 intensity, 14 2D LTEM, 2 GLRL, 1 NGTM) extracted from the MR scans were significant between SUV zones, and thus potentially of use in the distinction between MPNST and BPN. Further analysis showed a high correlation among the Law's kurtosis features and k-medoids clustering was implemented to identify 2 independent representative features. Fig. 4 shows box-plots of the final nine statistically significant features in T1 and T2 MR scans. The independent MPNST case with SUV_{max} of 3.4 showed split concordance with PET-hot and PET-elevated features; the T2 intensity mean and T1 kurtosis showed values within one standard deviation of the PET-hot zone's means while the remaining features fell closer to those of the PET-elevated zones. From the features extracted from the PET-signal, four (2 intensity, 2 NGTM) were statistically significant between the PET-hot and PET-elevated regions of MPNST patients (Fig. 5). There were no significant features extracted from the CT acquired in the PET-CT. The power test on these features returned powers greater than 0.90 indicating greater than 90% likelihood in identifying the significant effect.

The comparison of the PET-elevated zones in the MPNST cohort to the BPN subjects showed 20 distinctive features (4 T1 kurtosis LTEM, 8 T2 skewness LTEM, 4 GLRL, 4 NGTM). Again, the texture

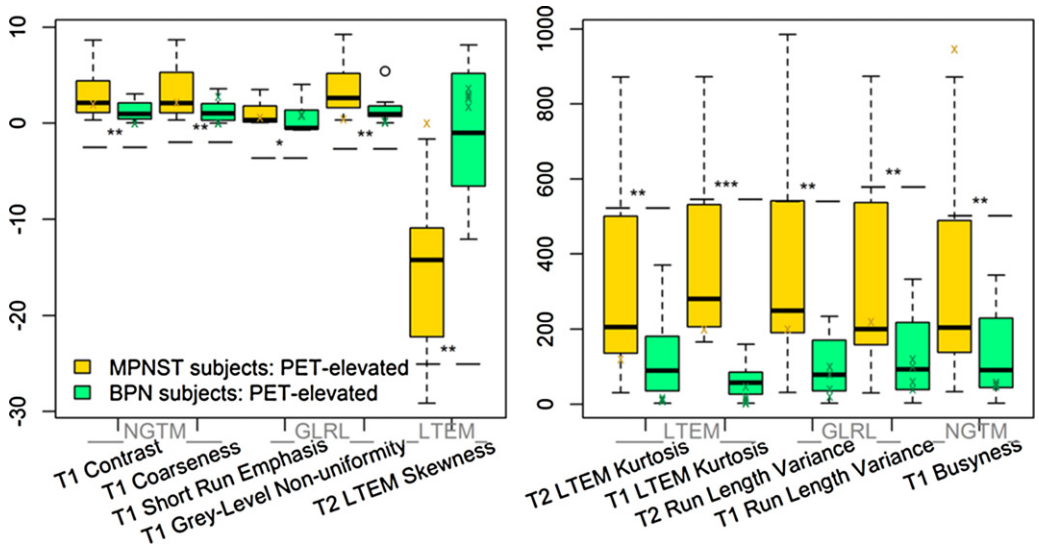

Fig. 4. Boxplot of significant MR features for PET-hot vs. paired PET-elevated regions. Image texture features (Law's texture energy measures [LTEM], grey-level run length texture [GLRL], and neighborhood grey-tone matrix texture [NGTM]) were extracted from the normalized dataset, these texture features do not typically have units associated with them. Significance: $^{*}0.02 < P \leq 0.05$, $^{**}0.005 < P \leq 0.02$, $^{***}P \leq 0.005$.

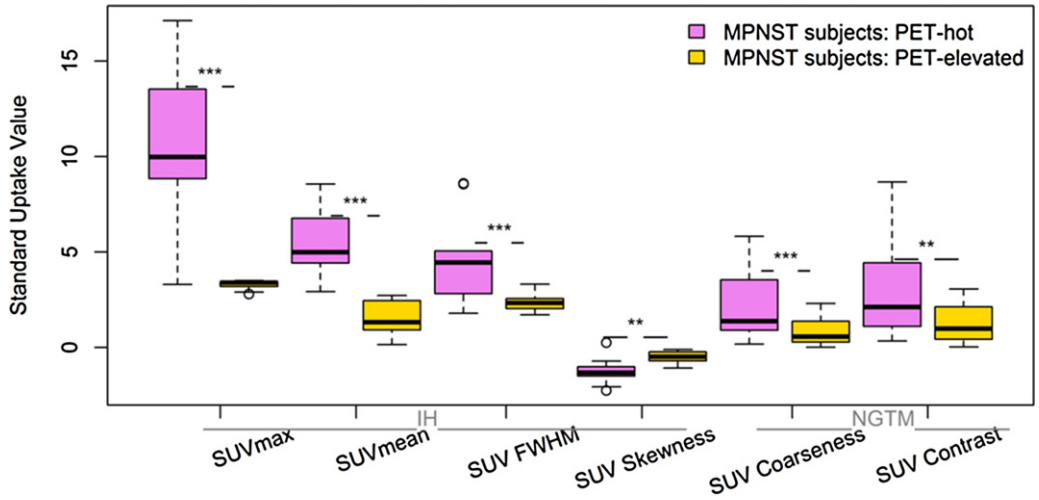

Fig. 5. Boxplot of significant PET features for PET-hot vs. paired PET-elevated regions. Image texture features (neighborhood grey-tone matrix texture [NGTM]) do not typically have units associated with them. Significance: $^{*}0.02 < P \leq 0.05$, $^{**}0.005 < P \leq 0.02$, $^{***}P \leq 0.005$.

features were tightly correlated; k-medoids clustering returned in a set of 10 unique features shown in boxplot form in Fig. 3. The independent cohort cases followed the general trends of their histopathology counterparts with the expectation of the MPNST's T2 LTEM skewness which was more than one standard deviation from the mean. From the radiomics extracted from the PET scan, eight (4 GLRL, 4 NGTM) were significantly different between the two subject groups (Fig. 6). The power test on these features returned powers greater than 0.94 indicating greater than 94% likelihood in identifying the significant effect.

Discussion

PNs can be composed of mosaic regions, therefore small or superficial biopsies may be inaccurate for the diagnosis of MPNST. Furthermore, surgery to remove or de-bulk the tumor comes with a high risk of nerve impairment, persistent pain, and other detrimental impact with regards to quality of life years. As this disorder largely affects children and adolescents, methods to increase the accuracy of non-invasive diagnostic procedures are urgently needed. In this study, PET SUV in conjunction with high resolution anatomical MR imaging allowed for the extraction of significant radiomic biomarkers from PN mosaic regions. We identified both a cohort of features which are statistically different in intra-plexiform comparison and a cohort of inter-plexiform features between subjects with different diagnoses. These findings are important as quantitative features are easily standardized and translationally relevant compared to qualitative interpretations.

Several studies have investigated qualitative MR radiologic features to aid in the differentiation between BPNs and MPNSTs: Matsumine ($n = 37$), Wasa ($n = 34$), Derlin ($n = 31$), Bhargava ($n = 16$), and Demehri ($n = 14$) [12–16]. Matsumine and Derlin had radiologists indicate irregular enhancement areas in T1-weighted MR imaging, both concluding the presence of inhomogeneous T1 signal was more common in MPNST cases [12–14]. In T2-weighted MR imaging, Matsumine and Bhargava showed mixed results with respect to presence of tumor target sign, a hyper-intense rim with centrally decreased intensity to muscle [12,15]. Matsumine, Wasa, and Derlin indicated the presence of intra-tumor cystic and lobulation characteristics to be proportionately higher in MPNST cases

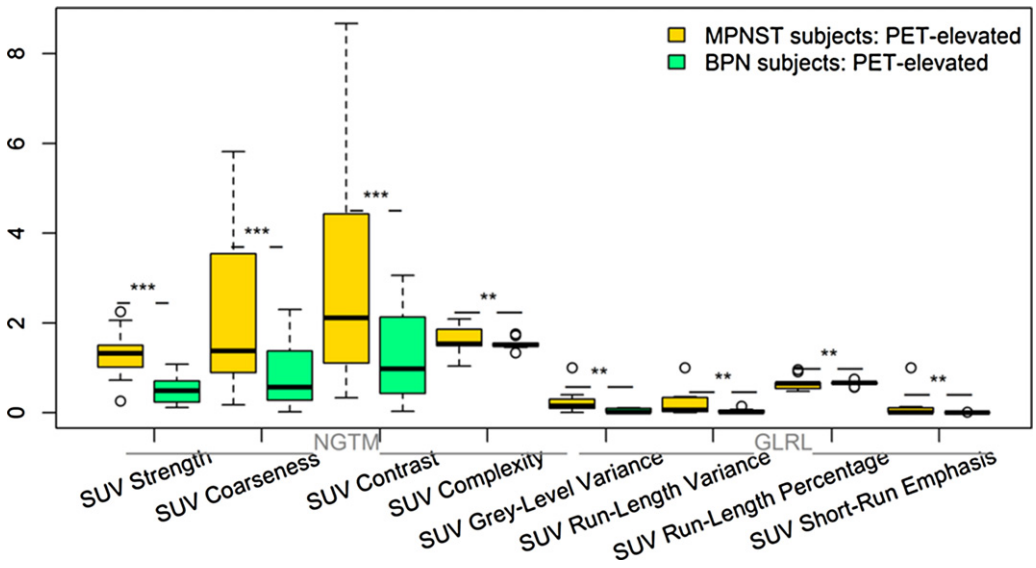

Fig. 6. Boxplot of significant PET features for PET-hot vs. paired PET-elevated regions. Image texture features (grey-level run length texture [GLRL] and neighborhood grey-tone matrix texture [NGTM]) do not typically have units associated with them. Significance: $^{*}0.02 < P \leq 0.05$, $^{**}0.005 < P \leq 0.02$, $^{***}P \leq 0.005$.

[12–14]. The tumor margin type (well-defined, ill-defined) was investigated by Matsumine, Derlin, and Demehri leading to conclusions about diffuse and well-circumscribed PN being likely MPNST and BPN, respectively [12,14,16]. Looking beyond the PN, Wasa and Demehri investigated the higher presence of peritumoral edema, or abnormal accumulation of fluid in the surrounding tissues, in MPNST cases over BPNs [13,16]. Building upon these qualitative imaging assessments, this study sought to determine if quantitative image based features, previously developed and proven in the distinction of malignant and benign lung tumors in CT [29], could be distinguishing of MPNST versus BPN. As quantitative features are automatically and algorithmically extracted these features could be applied in the future to computer-aided diagnosis tools in a similar manner to lung tumors.

This study demonstrates the potential for quantitative imaging features to be extracted from local MR imaging and used to investigate PN composition, based on glucose uptake values. While not powerful enough to develop a robust PN classifier, the nine MR intra-PN features between PET-hot and PET-elevated regions of MPNST subjects can be related back to the previously described qualitative features [12–16]. The inhomogeneity and lobulated appearance indicated by radiologists could be explained by the higher T2 intensity entropy, higher texture busyness, and lower intensity kurtosis in MPNST subjects. Similarly, the features with differences been the BPN cohort and the PN from the MPNST cohort could be useful in distinguishing subjects at risk for development of MPNST. The MR radiomic features described here could further increase in biological accuracy with the development of emerging MR acquisition methods which facilitated quantitative studies, such as MR fingerprinting and synthetic MRI [30–32].

Assessment using PET-signal is a growing area of interest in the differentiation between symptomatic BPNs and MPNSTs. This includes the aforementioned standard measurements such as SUV_{max} [5,7,8,33–38], liver-to-tumor ratio[8,34,39], metabolic tumor burden [5,33,34,40], as well as measures of tumor heterogeneity [33,34,37]. Salamon investigated a categorical binning of uptake heterogeneity and a quantitative measure of heterogeneity of the tumor showing both SUV_{max} and SUV_{mean} measures achieved high specificity (82.9% and 79.3% respectively) when optimizing for diagnostic sensitivity [33]. The same quantitative heterogeneity index was used by Van Der Gucht to differentiate 49 plexiform neurofibromas based on diagnosis, achieving an AUC of 0.67 [34]. Cook compared 14 quantitative PET features containing first order, second order, and high order PET texture measures determining while ^{18}F-FDG uptake is more heterogeneous in MPNSTs, there is no improvement over SUV_{max} in discriminative performance [37]. Our study found comparable results in the twelve PET-derived radiomic biomarkers to previously published results, with SUV_{max}, and high order measures displaying differences between MPNST and BPN subjects. The quantitative assessment of the CT did not yield any distinguishing features; however, this could be explained based on the quality of CT analyzed. We extracted features from the CT acquired with the PET, which is a low-dose scan used clinically for the PET-signal attenuation correction. It is possible with a higher quality CT, features within the PN could be better differentiated. As this disease presents higher risks from radiation exposure, the use of non-human models could offer the potential to find the optimal scanning parameters for MPNST differentiation [41–43].

The segmentation pipeline developed here performed well on cases where the PN was well-circumscribed, not diffuse. Armed with these promising results defining differences in the quantitative features extracted from MR, further improvements in the segmentation pipeline can be made to achieve more accurate PET-CT MR alignment and PN segmentation. The PET-based segmentation provided a systemic way to interrogate different zones of the PN; however six cases were excluded from the segmentation pipeline due to non-standard tissue enhancement. These cases served as an independent validation cohort demonstrating the potential strength of fused PET-MR data for heterogeneous PN analysis. In this study, registration, segmentation, and feature extraction took an average of 5.4 minutes per patient; an integrated PET-MR system would eliminate the need for registration, thereby decreasing time to less than 10 seconds per patient. Further, with the development of integrated PET-MR imaging systems, ideally suited for this subject population, there is direct potential for this method is to increase the sensitivity and specificity of clinical scans [44].

NF1 is a rare disorder and therefore many studies, including this one, contain small sample sizes (N ranging from 14 to 37) [12–16]. Yet even with a limited cohort, we have been able to identify a set of features distinctive between MPNST and PN regions. As our inclusion criteria required an accompanying PET-CT of the PN, we recognize there could be a bias in this cohort over examining all patients with PN imaging studies. The mosaic quality of PNs

could reduce the efficiency of imaging features extracted from the PN as a whole compared to regions extracted based on different functional qualities (PET-hot vs. PET-elevated). Furthermore, the clinical diversity of MR scanning parameters could affect extracted features; this study performed patient-scan normalization of quantitative features to muscle to reduce the effect of variations. With the discovery of distinguishing quantitative imaging features, this study warrants further exploration of segmentation and automated feature extraction independent of PET-signal. Ultimately, we aim to discover quantitative imaging features extracted from routine scans which will promote detection of MPNST and potentially decrease the number of invasive procedures for NF1 patients.

Conclusions

We identified both a cohort of features which are statistically different intra-plexiform and a cohort of inter-plexiform features between subjects with and without MPNST. As quantitative features are more easily standardized and translational than their qualitative counterparts, this study defines a base set of radiomic biomarker features which could aid in PN clinical assessment.

Disclosure of interest

The authors declare that they have no competing interest.

Appendix A. Supplementary data

Supplementary data associated with this article can be found, in the online version, at: https://doi.org/10.1016/j.neurad.2018.05.006.

References

[1] Kresak JL, Walsh M. Neurofibromatosis: a review of NF1, NF2, and schwannomatosis. J Pediat Genet 2016;5:98–104.
[2] Gutmann DH, Aylsworth A, Carey JC, et al. The diagnostic evaluation and multidisciplinary management of neurofibromatosis 1 and neurofibromatosis 2. JAMA 1997;278:51–7.
[3] Anderson JL, Gutmann DH. Chapter 4 - Neurofibromatosis type 1. In: Monica PI, Roach ES, editors. Handbook of clinical neurology. Elsevier; 2015. p. 75–86.
[4] Dombi E, Ardern-Holmes SL, Babovic-Vuksanovic D, et al. Recommendations for imaging tumor response in neurofibromatosis clinical trials. Neurology 2013;81:S33–40.
[5] Salamon J, Papp L, Toth Z, et al. Nerve sheath tumors in neurofibromatosis type 1: assessment of whole-body metabolic tumor burden using F-18-FDG PET/CT. PloS one 2015;10 [e0143305].
[6] Treglia G, Taralli S, Bertagna F, et al. Usefulness of whole-body fluorine-18-fluorodeoxyglucose positron emission tomography in patients with neurofibromatosis type 1: a systematic review. Radiol Res Pract 2012;2012:431029.
[7] Ferner RE, Golding JF, Smith M, et al. [^{18}F]2-fluoro-2-deoxy-D-glucose positron emission tomography (FDG PET) as a diagnostic tool for neurofibromatosis 1 (NF1) associated malignant peripheral nerve sheath tumours (MPNSTs): a long-term clinical study. Ann Oncol 2008;19:390–4.
[8] Salamon J, Veldhoen S, Apostolova I, et al. ^{18}F-FDG PET/CT for detection of malignant peripheral nerve sheath tumours in neurofibromatosis type 1: tumour-to-liver ratio is superior to an SUVmax cut-off. Eur Radiol 2014;24:405–12.
[9] Weizman L, Helfer D, Ben Bashat D, et al. PNist: interactive volumetric measurements of plexiform neurofibromas in MRI scans. Int J Comput Assist Radiol Surg 2014;9:683–93.
[10] Solomon J, Warren K, Dombi E, et al. Automated detection and volume measurement of plexiform neurofibromas in neurofibromatosis 1 using magnetic resonance imaging. Comput Med Imaging Graph 2004;28:257–65.
[11] Cai W, Kassarjian A, Bredella MA, et al. Tumor burden in patients with neurofibromatosis types 1 and 2 and schwannomatosis: determination on whole-body MR images. Radiology 2009;250:665–73.
[12] Matsumine A, Kusuzaki K, Nakamura T, et al. Differentiation between neurofibromas and malignant peripheral nerve sheath tumors in neurofibromatosis 1 evaluated by MRI. J Can Res Clin Oncol 2009;135:891–900.
[13] Wasa J, Nishida Y, Tsukushi S, et al. MRI features in the differentiation of malignant peripheral nerve sheath tumors and neurofibromas. AJNR Am J Roentgenol 2010;194:1568–74.
[14] Derlin T, Tornquist K, Munster S, et al. Comparative effectiveness of ^{18}F-FDG PET/CT versus whole-body MRI for detection of malignant peripheral nerve sheath tumors in neurofibromatosis type 1. Clin Nucl Med 2013;38:e19–25.
[15] Bhargava R, Parham DM, Lasater OE, et al. MR imaging differentiation of benign and malignant peripheral nerve sheath tumors: use of the target sign. Pediatr Radiol 1997;27:124–9.
[16] Demehri S, Belzberg A, Blakeley J, et al. Conventional and functional MR imaging of peripheral nerve sheath tumors: initial experience. AJNR Am J Neuroradiol 2014;35:1615–20.
[17] Yip SSF, Liu Y, Parmar C, et al. Associations between radiologist-defined semantic and automatically computed radiomic features in non-small cell lung cancer. Sci Rep 2017;7:3519.
[18] Fedorov A, Beichel R, Kalpathy-Cramer J, et al. 3D Slicer as an image computing platform for the quantitative imaging network. J Magn Reson Imaging 2012;30:1323–41.
[19] Yoo TS, Ackerman MJ, Lorensen WE, et al. Engineering and algorithm design for an image processing API: a technical report on ITK-the insight toolkit. Studies in health technology and informatics; 2002. p. 586–92.
[20] Styner M, Brechbuhler C, Szckely G, et al. Parametric estimate of intensity inhomogeneities applied to MRI. IEEE Trans Med Imaging 2000;19:153–65.
[21] Collewet G, Strzelecki M, Mariette F. Influence of MRI acquisition protocols and image intensity normalization methods on texture classification. Magn Reson Imaging 2004;22:81–91.
[22] Somer EJ, Benatar NA, O'Doherty MJ, et al. Use of the CT component of PET-CT to improve PET-MR registration: demonstration in soft-tissue sarcoma. PhysMed Biol 2007;52:6991–7006.
[23] Laws KI. Rapid texture identification. 24th annual technical symposium: International Society for Optics and Photonics; 1980. p. 376–81.
[24] Haralick RM, Shanmugam K. Textural features for image classification. IEEE Trans Syst Man Cybern 1973;3:610–21.
[25] Amadasun M, King R. Textural features corresponding to textural properties. IEEE Trans Syst Man Cybern 1989;19:1264–74.
[26] Jarque CM, Bera AK. A test for normality of observations and regression residuals. Int Stat Rev 1987;55:163–72.
[27] Levene H. Robust tests for equality of variances. Contrib Probability Stat 1960;1:278–92.
[28] Kaufman L, Rousseeuw P. Clustering by means of medoids. North-Holland: Elsevier; 1987. p. 405–16.
[29] Dilger SK, Uthoff J, Judisch A, et al. Improved pulmonary nodule classification utilizing quantitative lung parenchyma features. J Med Imaging (Bellingham Wash) 2015;2 [041004].
[30] Chen Y, Jiang Y, Pahwa S, et al. MR fingerprinting for rapid quantitative abdominal imaging. Radiology 2016;279:278–86.
[31] Ma D, Gulani V, Seiberlich N, et al. Magnetic resonance fingerprinting. Nature 2013;495:187–92.
[32] Tanenbaum LN, Tsiouris AJ, Johnson AN, et al. Synthetic MRI for clinical neuroimaging: results of the Magnetic Resonance Image Compilation (MAGiC) prospective, multicenter. Multireader Trial. AJNR Am J Neuroradiol 2017;38:1103–10.
[33] Salamon J, Derlin T, Bannas P, et al. Evaluation of intratumoural heterogeneity on (1)(8)F-FDG PET/CT for characterization of peripheral nerve sheath tumours in neurofibromatosis type 1. Eur J Nuclear Med Mol Imaging 2013;40:685–92.
[34] Van Der Gucht A, Zehou O, Djelbani-Ahmed S, et al. Metabolic tumour burden measured by 18F-FDG PET/CT predicts malignant transformation in patients with neurofibromatosis Type-1. PloS one 2016;11 [e0151809].
[35] Moharir M, London K, Howman-Giles R, et al. Utility of positron emission tomography for tumour surveillance in children with neurofibromatosis type 1. Eur J Nuclear Med Mol Imaging 2010;37:1309–17.
[36] Warbey VS, Ferner RE, Dunn JT, et al. [^{18}F]FDG PET/CT in the diagnosis of malignant peripheral nerve sheath tumours in neurofibromatosis type-1. Eur J Nuclear Med Mol Imaging 2009;36:751–7.
[37] Cook GJR, Lovat E, Siddique M, et al. Characterisation of malignant peripheral nerve sheath tumours in neurofibromatosis-1 using heterogeneity analysis of ^{18}F-FDG PET. Eur J Nuclear Med Mol Imaging 2017;44:1845–52.
[38] Benz MR, Czernin J, Dry SM, et al. Quantitative F^{18}-fluorodeoxyglucose positron emission tomography accurately characterizes peripheral nerve sheath tumors as malignant or benign. Cancer 2010;116:451–8.
[39] Combemale P, Valeyrie-Allanore L, Giammarile F, et al. Utility of 18F-FDG PET with a semi-quantitative index in the detection of sarcomatous transformation in patients with neurofibromatosis type 1. PloS one 2014;9 [e85954].
[40] Broski SM, Johnson GB, Howe BM, et al. Evaluation of (^{18})F-FDG PET and MRI in differentiating benign and malignant peripheral nerve sheath tumors. Skeletal Radiol 2016;45:1097–105.
[41] LaFemina J, Qin LX, Moraco NH, et al. Oncologic outcomes of sporadic, neurofibromatosis-associated, and radiation-induced malignant peripheral nerve sheath tumors. Ann Surg Oncol 2013;20:66–72.
[42] Meyerholz DK, Ofori-Amanfo GK, Leidinger MR, et al. Immunohistochemical markers for prospective studies in neurofibromatosis-1 porcine models. J Histochem Cytochem 2017 [22155417729357].
[43] White KA, Swier VJ, Cain JT, et al. A porcine model of neurofibromatosis type 1 (NF1) that mimics the human disease, JCI Insight, 2018: 3. [JCI insight Under revision at JCI Insight E-pub ahead of print https://www.ncbi.nlm.nih.gov/pubmed/29925695].
[44] Jena A, Taneja S, Jha A, et al. Multiparametric evaluation in differentiating glioma recurrence from treatment-induced necrosis using simultaneous (18)F-FDG-PET/MRI: a Single-Institution Retrospective Study. AJNR Am J Neuroradiol 2017;38:899–907.